Microwave and tunable far-infrared laser spectroscopy of the ammonia–water dimer

Paul A. Stockman,[a] Roger E. Bumgarner,[b] Sakae Suzuki,[a] and Geoffrey A. Blake[b,c]
California Institute of Technology, 170-25, Pasadena, CA 91125

(Received 14 August 1991; accepted 5 November 1991)

Microwave and far-infrared spectra of the H_3N–HOH dimer have been recorded from 36 to 86 GHz and 520 to 800 GHz with a planar supersonic jet/tunable laser sideband spectrometer. The *a*-type pure rotational microwave data extend the previous $m = 0$, $K = 0$ A symmetry manifold measurements of Herbine and Dyke [J. Chem. Phys. **83**, 3768 (1980)] to higher frequency and also provide an additional set of microwave transitions in the $mK = +1$ E symmetry manifold. Two sets of five *b*-type rotation–tunneling bands, one set shifted from the other by an approximately constant 113 MHz, have been observed in the far infrared. The splitting into two sets arises from water tunneling, while the overall band structure is due to internal rotation of the ammonia top. Nonlinear least-squares fits to an internal rotor Hamiltonian provided rotational constants, and an estimation of $V_3 = 10.5 \pm 5.0\ \mathrm{cm}^{-1}$ for the barrier height to internal rotation for the NH_3 monomer. A nonlinear *equilibrium* hydrogen bond is most consistent with the vibrationally averaged rotational constants; with the angle $\cos^{-1}[\langle\lambda_z\rangle]$ determined from $\langle\lambda_z\rangle$, the projection of the ammonia's angular momentum onto the framework; and with the nitrogen quadrupole coupling constants of Herbine and Dyke. The water tunneling splitting and observed selection rules place constraints on the barrier height for proton exchange of the water as well as the most feasible water tunneling path along the intermolecular potential energy surface. An estimated barrier of $\sim 700\ \mathrm{cm}^{-1}$ is derived for the water tunneling motion about its *c* axis.

I. INTRODUCTION

Hydrogen bonds and van der Waals interactions are ubiquitous in biologically important macromolecules, such as proteins and polynucleic acids, and determine much of their three-dimensional structure and folding dynamics. A large subset of these weak bonds are between nitrogen and oxygen containing moieties and nearby protons from similar species. Multiple possibilities for hydrogen bond donor and acceptor roles exist, and preferences among these roles arise from the subtle effects of both chemical substitution and steric environment. The effects of substitution and local environment are important to consider when generalizing or extrapolating from one system to another. For example, the double helices of DNA contain repetitions of proton donation from amides and amines to carbonyls and other amides, and proton donation *from* amides and amines is a common theme in biology. Donations of hydrogen bonds from amides have been observed in gas phase dimers of formamide with water and methanol by Lovas *et al.*[1] For these, the nitrogen of formamide and the oxygen of either water or methanol act simultaneously as hydrogen bond acceptors, resulting in a cyclic structure with two hydrogen bonds. However, for gas phase ammonia, the "simplest amine," the preference for hydrogen bonding is, without an observed exception, for the acceptance of protons.[2] Given this difference in acceptor/donor preference between gas phase ammonia and amine functional groups in solution, either the structures of sterically constrained amine hydrogen bonds do not reflect potential minima of the unconstrained functional groups or carbon bound amines interact significantly differently than unsubstituted ammonia.

Hydrogen bonds are also important cosmochemically. In a gas of solar composition, the most stable carbon, nitrogen, and oxygen containing species at the temperatures and pressures which characterize protostellar nebulae are methane, ammonia, and water. Ices, hydrates, and clathrates formed from these and other species, most notably CO, N_2, and the noble gases, may therefore play critical roles in the origin and evolution of outer solar system bodies.[3] For example, in the Saturnian system it has been estimated that the initial ice budgets of Titan as well as the smaller satellites may have contained as much as 15% ammonia–water hydrate.[4] The coexistence of a number of hydrate–clathrate systems determines, in part, the volatile inventories of comets, icy satellites, and other objects; and a detailed understanding of their formation kinetics, phase diagrams, and mechanical properties is essential over a wide range of temperatures and pressures. Accurate experimental measurements sampling the entire parameter space provided by cosmochemical environments are exceedingly difficult. Theoretical models have therefore remained the principal means of addressing the importance of ices in the early solar system.[5]

In order to correctly model large molecules, solutions, and ices, accurate pair-wise as well as many-body intermolecular potentials are needed for a wide variety of functional

[a] Division of Chemistry and Chemical Engineering.
[b] Division of Geological and Planetary Sciences.
[c] Presidential Young Investigator, Sloan Fellow, Packard Fellow.

 0021-9606/92/042496-15$06.00

group interactions. Such potentials are required over the *full* range of possible angles and distances so that the relative trade offs between forces of similar magnitude can be properly calculated. The theoretical calculation of realistic anisotropic potentials for such systems is a formidable challenge, and drastic assumptions are typically invoked in simulations of macroscopic materials and biological macromolecules. Indeed, popular molecular mechanics or quantum mechanics programs such as AMBER,[6] Biograf,[7] CHARM,[8] and MM2[9] make use of tables of empirical parameterizations of nonbonded potentials either as the only treatment of such interactions or as the starting point for subsequent higher level calculations. Often times, the parameterizations employed assume that a given atom's nonbonded interaction with another atom is independent of the local environment or substitution of the atoms involved. That is, all amine–hydroxyl group interactions are identically parameterized regardless of what either functional group is bound to.

Experimentally, the detailed spectroscopic study of isolated weakly bound clusters in supersonic jets has become an important tool in the characterization of the simplest intermolecular potential energy surfaces (IPS). However, the most commonly employed methods, rotational spectroscopy at microwave frequencies with MBER[10] or Flygare–Balle instruments,[11] typically sample only the region of the IPS near the equilibrium structure. High resolution vibrational and electronic spectroscopy of *intra*molecular modes in the IR[12] and visible/UV[13] yields more extensive sampling of the IPS, especially for the most weakly bound complexes for which combination and hot bands often possess considerable intensity. Such studies also provide insights into the extremely interesting dynamics which take place when weakly bonded clusters are excited into their dissociative continua. However, none of the above-mentioned methods are direct probes of the *inter*molecular modes which occur at far-infrared (FIR) wavelengths, and which most directly sample the IPS in the *intra*molecular ground state.

We have therefore undertaken a program aimed at the understanding and accurate parameterization of van der Waals and hydrogen bonding interactions between various functional groups via FIR laser spectroscopy of vibration–rotation–tunneling (VRT) bands of van der Waals and hydrogen bonded clusters in planar supersonic free jet expansions. Studies of this type have only recently become technologically feasible, but have been shown to be an important new tool in the characterization of the IPS for simple clusters such as Ar–HCl,[14] Ar–H_2O,[15] $(HCl)_2$,[16] etc. Here the ammonia–water dimer was chosen as a prototypical example of proton donation from the simplest hydroxyl group to the simplest amine. This dimer continues our study of the FIR spectroscopy of weakly bound dimers of water with other molecules of atmospheric, biochemical, and cosmochemical importance: Ar–DOH/DOD,[17] OC–HOH,[18] N_2–HOH,[19] and C_6H_6–H_2O.[20] This study also compliments a series of investigations by others of water-containing dimers, $(H_2O)_2$,[21] Ar–HOH,[15,22] OC–HOH,[23] N_2–HOH,[24] and CH_4–HOH,[25] as well as a much larger body of work in the microwave and IR on weakly bound clusters.[10–13,26]

In Fig. 1, the ammonia–water dimer is diagrammed in a

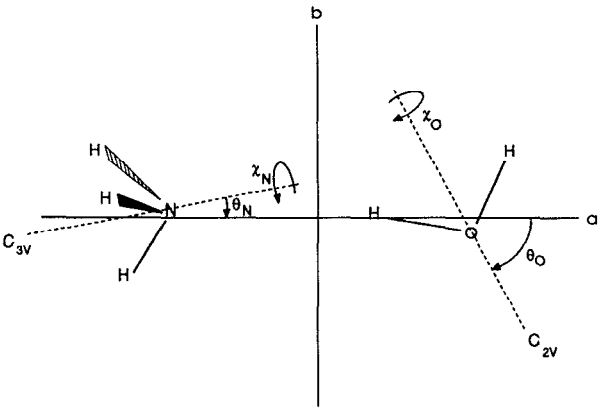

FIG. 1. Coordinate system for the ammonia–water dimer. The angles ϕ_N and ϕ_O are not shown but are the angles the C_{3v} and C_{2v} axes make with the a–b plane.

principal axis coordinate system with the a axis nearly colinear to the line connecting the centers of mass of the ammonia and water monomers. From inspection, two low frequency and large amplitude internal motions can be expected, and indeed are observed. As in other ammonia-containing dimers, e.g., CO_2–,[27] N_2O–,[28] CF_3H–,[29] and CH_3OH–NH_3,[30] the ammonia monomer can rotate about its C_{3v} symmetry axis in a fairly low barrier potential. The water monomer also experiences internal tunneling of its protons in a double minimum potential. These large amplitude motions greatly complicate the spectra, which in turn increases the number of terms in the Hamiltonian needed to accurately describe the energy levels. Small molecules with large amplitude motions, such as ammonia–water dimer, provide a challenge to spectroscopists to develop realistic Hamiltonians which accurately describe them. For the most weakly bound atom–molecule dimers, the full calculation of the VRT eigenvalues from an adjustable IPS have proven to be the most direct route to an understanding of their spectra,[14,15] but for strongly bound systems such as ammonia–water a more conventional approach remains a useful starting point.

Ammonia–water dimer has been the subject of a microwave and radio frequency molecular beam electric resonance study by Herbine and Dyke[31] (hereafter HD), matrix infrared work by Nelander *et al.*,[32] and several *ab initio* calculations.[33] The ground state rotational, Stark effect, and nitrogen quadrupole coupling data of HD yielded rotational constants and dipole moments as well as a mostly determined structure. In a later paper on H_3N–H_2S,[34] Herbine *et al.* reported the measurement of several radio frequency transitions in the $m = 1$, $K = 1$ E state of H_3N–HOH. The matrix isolation studies of ammonia and water in Ne, Ar, and Kr by Nelander *et al.*[32] detected vibrational fundamentals for both the perturbed ammonia and water intramolecular modes and for several of the intermolecular modes of the dimer. The most recent *ab initio* work of Latajka and Scheiner[33] employed a fairly large basis set, treated correlation at the MP2 level, corrected for basis set superposition error and fully optimized the structure. In addition, vibra-

tional frequencies and intensities were calculated and used as a guide to interpret some of the unassigned bands of the matrix IR work. We record here measurement of ten low lying rotation–tunneling bands in the FIR, the observation of a new set of microwave transitions and the extension of previous microwave data to higher frequency. In what follows, we present a discussion of the experimental techniques and fitting procedures employed. We then close with an interpretation of the results.

II. EXPERIMENT

Both the microwave and FIR spectra were measured in the same planar expansion. The Caltech tunable FIR sideband spectrometer, described below, is an offspring of the parent Berkeley apparatus.[35] This in turn was a modification of the design by Pickett and co-workers,[36] who also provide a brief overview of previous tunable FIR sources. A recent review of tunable FIR spectrometers and a detailed discussion of the operating principles and design of the Berkeley instruments may be found in Refs. 37 and 38. The direct absorption microwave spectrometer has been previously documented,[39] so only the details pertinent to the present discussion will be outlined here.

A block diagram of the Caltech tunable FIR spectrometer is shown in Fig. 2. The FIR laser is home built and consists of a 2.5 m jacketed, water cooled pyrex tube with a 1.5 in. o.d. The laser tube projects into sealed aluminum boxes on either end which contain cavity end mirrors and stepper motor adjusted mounts. The laser resonator consists of gold coated 2.0 in. o.d. flat copper mirrors cooled by thermal contact with a block in the mount through which water is circulated. The input end mirror has a 5.0 mm beveled hole cut into it in order to allow the CO_2 pump radiation into the cavity, while the output end mirror has a beveled 10.0 mm hole blocked by a coated quartz output coupler which reflects the CO_2 pump radiation and lets about 20% of the FIR radiation pass. A 150 W cw CO_2 laser from Apollo Lasers Inc. coaxially pumps the FIR laser. The output from the FIR laser is about 0.7 W on the 118 μm CH_3OH line and better than 50 mW on many lines from 70–700 μm.

The FIR laser output is mixed with microwaves in a corner cube mixer (constructed from in-house designs by Custom Microwave) which incorporates a University of Virginia 117 GaAs Schottky barrier diode. Phase-locked microwave radiation is produced by a Wiltron model 6747A-20 frequency synthesizer operating between 0.1 and 20.0 GHz, with a maximum output power of + 18 dBm. Various solid state multipliers and amplifiers are used to produce frequencies up to 83 GHz with output powers no lower than 0 dBm. Mixing of the microwave and FIR laser signals by the diode produces tunable laser sidebands at $\nu_{\text{laser}} \pm n \cdot \nu_{\text{microwave}}$, where n is an integer. Strong transitions have been seen on $n = 4$, but the most sideband power is produced for $n = 1$. We estimate that our $n = 1$ sideband power ranges from 10 up to 100 μW on the strongest laser lines.

The tunable sidebands are separated from the considerably more intense laser carrier by a polarizing diplexer of the Martin and Puplett design.[40] They are then collimated and

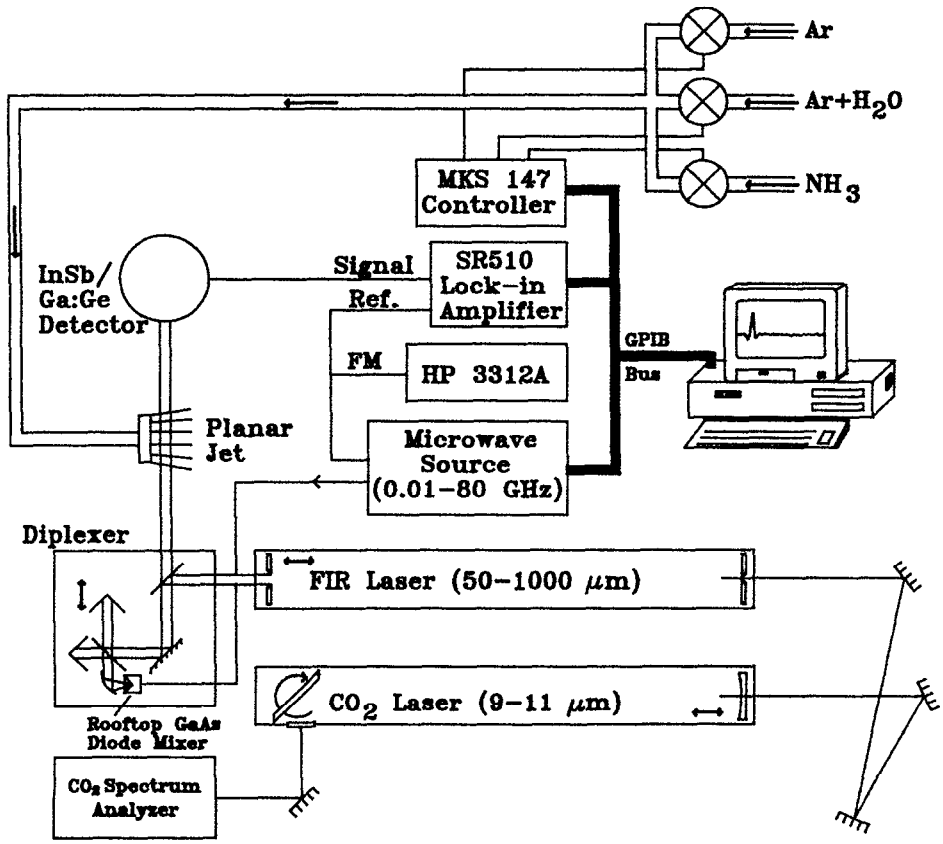

FIG. 2. Block diagram of the tunable far-infrared laser sideband spectrometer.

focused through the plane of a supersonic jet with a 2 cm focal length lens. The laser beam is then recollimated with an identical lens on the output side of the vacuum chamber and directed onto an InSb hot electron bolometer (Cochise Instruments) held at $He_{(l)}$ temperature, whose output is amplified and passed to a Stanford Research Systems model SR510 lock-in amplifier. Frequency modulation of the Wiltron at 50 kHz with a typical deviation of 300 kHz produces an equivalent modulation in the laser sidebands. The lock-in detector is referenced to twice the modulation frequency, yielding a second derivative signal.

The supersonic jet is a slit nozzle of dimension 0.001 in. $\times$ 1.75 in., identical in design to the Berkeley nozzle.[35] An Edwards EH4200 Roots blower backed by two Edwards E2M275 mechanical pumps evacuates the chamber containing the nozzle. The pumps are connected to the system by about 100 feet of 12 in. diameter stainless steel pipe, yielding a net pumping speed of 2000 cfm. Four MKS model 1259B mass flow controllers under the control of an MKS model 147B mass flow programmer regulate the flow of the component gases prior to mixing and exit through the nozzle.

The frequency synthesizer, lock-in amplifier and mass flow programmer are under the control of an Everex System 1800 computer (AT clone) via a National Instruments GPIB (IEEE-488) bus. Software written in MicroSoft Quick Basic turns on the gas, steps the frequency synthesizer, reads data from the lock-in and displays the spectrum in real time on the computer monitor. Scans taken with the gas off may be subtracted to remove baseline features due primarily to resonances in the microwave transmission lines. Data may also be taken in an automated mode. In this mode, no operator is needed and sequential, slightly overlapping frequency windows are saved on disk for subsequent viewing. Due to instabilities in the free running CO_2 laser (caused primarily by fluctuations in the cooling water temperature), the automated mode can currently be used only on the stronger, more stable FIR laser lines. This problem can be solved by the addition of a feedback loop which will adjust the CO_2 cavity length to maintain constant FIR output power.

The microwave absorption measurements were made in the region of 36 to 86 GHz, using the same frequency synthesizer, solid state multipliers, and amplifiers for the source. Radiation was fed into the focusing lens by means of a tapered wave guide horn and collected on the other side of the chamber with a similar horn. Transmitted power was detected by a Hewlett–Packard H06-R422A waveguide-mounted diode, the output of which passed to the lock-in amplifier. The microwave spectrometer is controlled with the same computer and software as the FIR spectrometer and is usually run in the completely automated mode. At centimeter and millimeter wavelengths, typical linewidths (FWHM) are 0.84 MHz, apparently limited by pressure broadening due to molecular beam interrogation close to the nozzle throat. For a scan rate of about 200 MHz/h, the average signal-to-noise ratio of the microwave transitions was about 25 to 1.

Spectra were collected from 520 to 800 GHz with the FIR laser tuned to the formic acid lines at 584.3882 or 692.9513 GHz. A few of the low frequency FIR transitions were measured with a Rollin mode (zero field) InSb detector, but the large majority of lines were recorded using a Putley mode InSb detector at a field strength of 5.5 kG. For the FIR transitions, typical linewidths were only slightly broader than those observed with the microwave apparatus, 1.0 MHz (FWHM), with the strongest lines having a signal-to-noise ratio of 1000 to 1.

Ammonia–water clusters were produced by passing a stream of technical grade Ar over deionized H_2O, which was combined approximately 1 m upstream from the nozzle with a second line containing $NH_{3(g)}$. A third line of pure Ar was also added at this juncture. Using separate lines for $Ar + H_2O$ and pure Ar allowed the water concentration to be adjusted at a fixed backing pressure simply by varying the relative flow rates rather than adjusting the temperature of the water. The evaporation of the water occurred at room temperature into a $\sim$4 psi (gauge) Ar stream. For both the microwave and the torsional ground state ($|m| \leqslant 1$) FIR measurements, a mixture of 1.116/3.427/0.0330 standard liters per minute (slm) $Ar/Ar + H_2O/NH_3$ was found to give a maximum absorbance. Signal intensity was found to be much more dependent upon maintaining a backing pressure of $\approx$500 Torr than upon the individual contributions of any of the gas flows. A lower flow rate of 2.000/0.0900 slm $Ar + H_2O/NH_3$ was used to observe torsionally hot FIR transitions ($|m| = 2$). This lowered the backing pressure to 250 Torr and raised the measured J-rotational temperature T_J from 4 to 12 K. By eliminating either the $Ar + H_2O$ or the NH_3 flows and compensating to the original backing pressure, signals due to ammonia, water, argon–ammonia, ammonia dimer, and argon–water species could be easily discerned from ammonia–water transitions.

III. SPECTRAL ANALYSIS

A. Hamiltonian

In the ammonia–water dimer, the ammonia monomer internally rotates about its C_{3v} axis and the water monomer tunnels between equivalent configurations in a double minimum potential. The three equivalent protons on ammonia and two equivalent protons on water, along with the "feasible" tunneling paths noted above, lead to a G_{12} permutation–inversion group for the dimer. The character and correlation tables for this group as applied to nitromethane and methylamine may be found in Bunker[41] and Ohashi and Hougen.[42] The irreducible representations of this group are A_1', A_1'', A_2', A_2'', E', and E''. The internal rotation of the ammonia monomer about its symmetry axis splits the rotational levels of the dimer into two separate manifolds, analogous to those associated with the torsional motions of methyl and silyl groups of other molecules: an A symmetry manifold for $m = 0$ mod 3 and an E symmetry manifold for the remaining levels. States in the A manifold pair with one of the ammonia proton spin functions, $I = 3/2$, while states in the E manifold pair with the $I = 1/2$ spin functions. The two water tunneling states (spatially symmetric and antisymmetric) are associated with each value of m leading to the prime and double prime labels. The pairing of the ortho and para

water spin functions with a given water tunneling function is determined by the symmetry of the rotational wave function and is discussed later.

Since the NH_3 internal rotation is a low barrier case and the H_2O tunneling is a high barrier case, the observed band positions are mostly determined by the internal rotation part of the Hamiltonian with a secondary small splitting due to the water tunneling. The elegant tunneling path approach developed for the water dimer by Hougen[43] and Coudert and Hougen[44] could, in principle, be used to fit matrix elements and tunneling splittings for both motions simultaneously, but is beyond the scope of the present work and hardly justified for the amount of data currently available for the H_3N–HOH complex. Here we have found it convenient to treat the problem as one of internal rotation in two separate water vibrational states. For an asymmetric top with a single threefold internal rotor, the Hamiltonian can be written as

$$\hat{H} = \hat{H}_{\mathrm{Rot}} + F(\mathbf{p} - \mathbf{P})^2 + (V_3/2)(1 - \cos 3\phi). \quad (1)$$

Here, $\hat{H}_{\mathrm{Rot}}$ is the standard asymmetric top rotational Hamiltonian, while F is the effective rotational constant for the internal motions of the ammonia rotor about its symmetry axis. F is calculated as follows:

$$F = h^2/(8\pi^2 r I_{\mathrm{top}}), \quad (2)$$

$$r = 1 - \sum_g I_{\mathrm{top}}\lambda_g/I_g, \quad g = (a,b,c) \text{ or } (z,x,y), \quad (3)$$

where I_{top} is the moment of inertia of the internal rotor about its symmetry axis, I_g is the moment of inertia of the molecule about the g principal axis, λ_g is the directional cosine between the symmetry axis of the top and the g axis, and $\mathbf{p} - \mathbf{P}$ is the relative angular momentum of the top and the frame. The derivation of the Hamiltonian may be found in Ref. 45. It is useful to examine some parts of the Hamiltonian and matrix elements in order to understand the spectrum. Hence, even though the matrix elements for the above Hamiltonian have been given in Ref. 46, they are reproduced here. $\hat{H}$ may be expanded to yield

$$\hat{H} = A'P_a^2 + B'P_b^2 + CP_c^2 - 2F(\alpha P_a p + \beta P_b p) + F\alpha\beta(P_a P_b + P_b P_a) + Fp^2 + V(\phi) + H_{\mathrm{dist.}}, \quad (4)$$

where

$$A' = A + F\alpha^2, \quad B' = B + F\beta^2,$$
$$\alpha = \lambda_a I_{\mathrm{top}}/I_a, \quad \beta = \lambda_b I_{\mathrm{top}}/I_b.$$

It has been assumed that λ_c is zero (i.e., the C_{3v} axis of NH_3 lies in the a–b plane). $H_{\mathrm{dist.}}$ contains quartic and hextic rotational distortion terms plus additional distortion terms which allow for changes in the rotational constants in the various internal rotor states. The nonzero matrix elements of the Hamiltonian used, Eq. (4), in the prolate top–free rotor basis are

$$\langle JKMm|\hat{H}|JKMm\rangle = A'K^2 + \tfrac{1}{2}(B' + C)[J(J+1) - K^2] - 2F\alpha Km + Fm^2 + V_3/2 + \text{quartic and hextic distortion terms}, \quad (5)$$

$$\langle JKMm|\hat{H}|JK \pm 1Mm\rangle = F\beta[\tfrac{1}{2}\alpha(2K \pm 1) - m][J(J+1) - K(K \pm 1)]^{1/2}, \quad (6)$$

$$\langle JKMm|\hat{H}|JK \pm 2Mm\rangle = \tfrac{1}{4}(B' - C)[J(J+1) - K(K \pm 1)]^{1/2}[J(J+1) - (K \pm 1)(K \pm 2)]^{1/2} + \text{quartic and hextic distortion terms}. \quad (7)$$

$$\langle JKMm|\hat{H}|JKMm \pm 3\rangle = -V_3/4. \quad (8)$$

The quartic and hextic distortion corrections used in Eqs. (5) and (7) are the standard terms of a Watson A-reduced Hamiltonian in the I_r basis.[47]

A few features of the above equations are particularly noteworthy. In Eq. (4), it can be seen that one of the effects of internal rotation is to modify the effective rotational constants about the principal axes for which λ_g is nonzero. The diagonal matrix element term of $-2F\alpha Km$ in Eq. (5) arises from the coupling of overall and internal rotation. For $mK \neq 0$, this term produces a large splitting, lowering the energy of states with a positive mK product and raising the energy of the states with a negative mK product, with the splitting being directly proportional to F and α. The result is that for b–dipole transitions in states with $mK \neq 0$, the P, Q, and R branches all terminate on degenerate levels. This situation greatly aids in the assignment of b–dipole spectra for $mK \neq 0$ states since ground state combination differences with a-dipole transitions can be formed between Q branches and P or R branches rather than just between P branches and R branches. A markedly different situation arises in a near prolate asymmetric top with a similar (B–C) value in that the P and R branch transitions terminate on the lower level of an asymmetry split doublet while Q branches terminate on the upper level. Since K_O is not a particularly useful quantum number for states with $m \neq 0$, we label all states with m, K_P, and mK_P. Also since we are very near the prolate limit, we will drop the prolate subscript from K_P. For $m = 0$ states, a negative value of K indicates the lower level of an asymmetry doublet.

B. Microwave data

Collisional cooling does not efficiently convert between spin states. Substantial populations in the lowest A' and A'' states ($m = 0, K = 0$) and the lowest E' and E'' states ($m = \pm 1, K = \pm 1, mK = +1$) are therefore produced in the molecular beam. Because the barrier to water tunneling is fairly high in this molecule (see Sec. V), there is very little difference in the vibrationally averaged structure of water tunneling states. Thus the $\Delta K = 0$ rotational transitions in the prime and double prime states (which do not cross the water tunneling splitting) are unresolved. We note that in both N_2–HOH[19,24] and OC–HOH,[18,23] where the barriers to water tunneling are smaller, the differences in the vibrationally averaged structures of the two water tunneling states produce observable splittings in the $\Delta K = 0$ transitions.

A total of 22 lines were observed in the microwave spectra, of which 7 were assigned and fit as transitions of

H_3N–HOH. Nine of the transitions appear to be hyperfine multiplets of the $J = 1$–2 transitions of the lowest E and A states and were not included in the fit. Several remaining lines do not lie particularly close to any predicted pure rotational transition of H_3N–HOH and have not yet been assigned. In the previous microwave work, HD observed a–dipole, $J = 0$–1, and $J = 1$–2 rotational transitions in the A states. We were able to extend the observations of these states higher in frequency, up to the $J = 5$–6 rotational transitions. We also observed an additional set of a–dipole transitions in the lowest E states. Both sets of transitions are presented in Table I.

TABLE I. Measured a–dipole (microwave) transition frequencies (MHz) for H_3N–HOH.

J'	K'	J''	K''	m	Measured	o–c[a]
3	0	2	0	0	36 852.32	0.08
4	0	3	0	0	49 132.44	−0.17
5	0	4	0	0	61 409.04	−0.44
6	0	5	0	0	73 681.02	−1.13
3	1	2	1	1	36 815.00	−0.53
4	1	3	1	1	49 082.70	−0.72
6	1	5	1	1	73 606.74	−1.41

[a] Calculated for $V_3 = 10.5\ cm^{-1}$.

C. Far-infrared data

In the FIR, a total of 289 transitions were observed which required the presence of both NH_3 and H_2O. Of these, 260 were assignable to H_3N–HOH transitions. Initial FIR searches in the 450–550 GHz range proved fruitless. At higher frequency were found six bands occurring in three pairs. The bands within each pair were separated by an almost constant 113 MHz, while the spacing between the pairs was wider and on the order of 10 GHz. All of the bands contained P, Q, and R branches with Q-branch origins for each pair located approximately at 633, 643, and 653 GHz. Stick spectra of the Q branches of all the observed bands are shown in Fig. 3. In Fig. 4, an expanded view of the Q branches for the pair of bands at 633 GHz is presented. By inference to the structure determined by HD and because the 113 MHz splitting was approximately constant across all J's in all bands, this splitting was attributed to a tunneling effect of the water monomer. Also of note is the fact that in each pair of bands, one set of states was approximately three times stronger than the other, indicating that one band is associated with the ortho spin state of water while the other is associated with the para state. The additional splitting into three (and later we will see, five) bands is due to internal rotation of the ammonia group. Frequencies of the observed FIR transitions are given in Table II.

The bands at 643 and 633 GHz were assigned and matched with the microwave data by the method of combination differences. The two bands originating near 643 GHz matched with the states previously seen in the Dyke lab and the two bands near 633 GHz correspond to the new set of microwave transitions. The branches with origins at 643 GHz were $K = 0 \rightarrow 1$ in character and were assigned to the A state($m'',K'',m''K'' \rightarrow m',K',m'K' = 0,0,0 \rightarrow 0, \pm 1,0$)transition while the bands at 643 GHz were $K = 1 \rightarrow 0$ and were

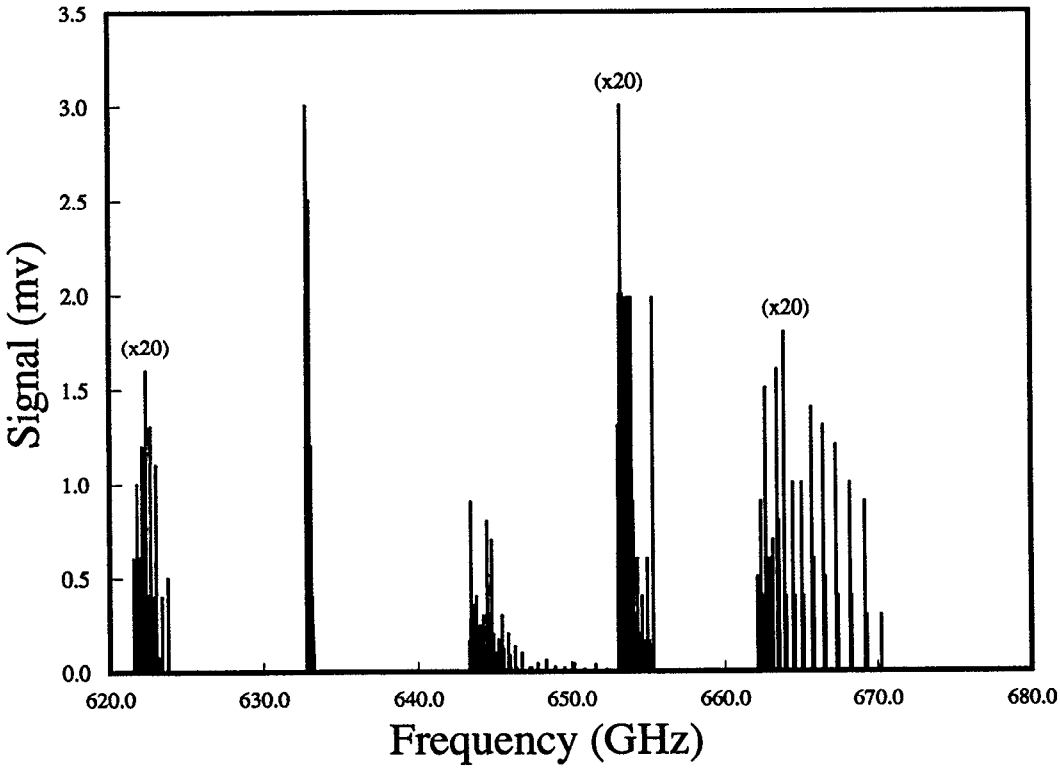

FIG. 3. Stick spectra of the observed FIR bands. For clarity, all P- and R-branch transitions have been removed and only the observed Q branches are shown. The intensities of the weaker bands have been increased by the factors indicated in the figure. Due to sideband power fluctuations, the relative intensities are only approximate.

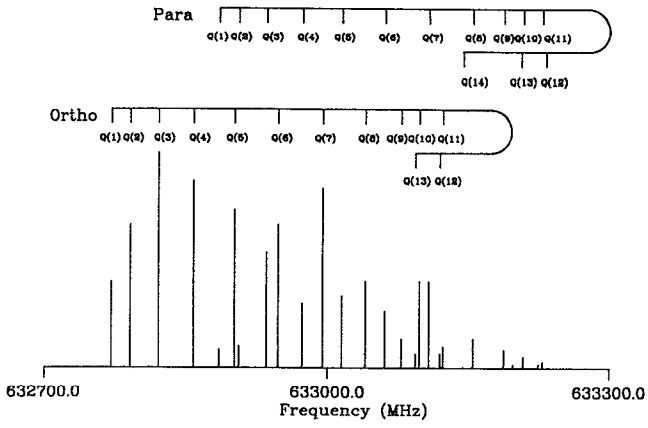

FIG. 4. An expanded view of the Q branches at 633 GHz showing the nearly constant 113 MHz water tunneling splitting and the approximate 3:1 intensity ratio. Ortho and para indicate the water tunneling state associated with each band. Due to sideband power fluctuations, the relative intensities are only approximate.

assigned as E state ($m'',K'',m''K'' \rightarrow m',K',m'K' = \pm 1, \pm 1, +1 \rightarrow \pm 1,0,0$) transitions. P branches of the bands at 653 GHz were very weak and initially precluded their detection and a definite assignment. The assigned bands (two per water tunneling state) were fit to the Hamiltonian of Eq. (5) in a nonlinear least squares fit. The basis set was factored into A and E symmetry blocks and truncated at $|K| = 4$ and $|m| = 9$. Numerical tests showed that the energy levels of interest had converged to better than 50 kHz with this size basis. In order to reproduce our data to near experimental uncertainty, we found it necessary to allow λ_x and λ_z to vary independently in the fits, as opposed to constraining the sum $\lambda_x^2 + \lambda_z^2$ to unity. There are two reasons for this. First, vibrational averaging will project a small amount of the internal top's angular momentum out of the x–z plane, and second, even in the limit of λ_y exactly zero, $\langle\lambda_x\rangle^2 + \langle\lambda_z\rangle^2 \neq 1$.

The constants obtained from a combined fit of the microwave data and the first four FIR bands were then used to predict an energy level diagram. From the calculated energy levels, we were able to assign the 653 GHz bands as $m'',K'',m''K'' \rightarrow m',K',m'K' = \pm 1, \pm 1, +1 \rightarrow \pm 1, \pm 2, +2$, find several P-branch transitions and include the bands into the fits. Our predicted energy level diagram also showed that the $m,K,mK = \pm 2, \pm 2, +4$ state was fairly low lying ($\sim$540 GHz above $m,K,mK = \pm 1, \pm 1, +1$) and had allowed transitions to the $m,K,mK = \pm 2, \pm 1, +2$ and $m,K,mK = \pm 2, \pm 3, +6$ states between 600 and 700 GHz. Since V_3 was not well determined from the data accessing only the $m = 0$ and $m = \pm 1$ states, a search was mounted for transitions from the $m,K,mK = \pm 2, \pm 2, +4$ state. By raising the beam temperature as described above from $T_J = 4$ to 12 K, these two transitions were indeed observed within 10 GHz of the predictions. Band origins occured at 621 and 662 GHz, again with separate bands for both water tunneling states split by $\sim$113 MHz. An energy level diagram for the internal rotor states, showing both the observed transitions and the predicted energies for higher states, is presented in Fig. 5.

Once the additional bands were added to the fit (now five bands per water tunneling state) we found that several extra distortion terms were required. Specifically, we needed to permit $(B + C)/2$ ($\overline{B}$) in the various m,K states and A in the $m = \pm 2$ states to vary relative to the $m = 0$ states. To accomplish this we added the following terms to the diagonal of the Hamiltonian matrix:

$$\langle JKMm|\hat{H}_{\text{int.dist.}}|JKMm\rangle = \Delta\overline{B}_{m,K,mK}J(J+1), \quad (9)$$

$$\langle JKM,\pm 2|\hat{H}_{\text{int.dist.}}|JKM,\pm 2\rangle = \Delta A_{m=2}K^2. \quad (10)$$

In addition, it was also necessary to allow Δ_K and Δ_J for the $m = \pm 2$ states to assume different values than in the $m = 0$ and $m = \pm 1$ states. When all the additional distortion parameters necessary to reproduce the data to near experimental accuracy were included, there were again high correlations between V_3, the terms multiplied by the various powers of K in Eqs. (5)–(7) and the λ's. Note that the additional distortion terms are for specific values of mK. A more standard approach is to include higher order terms of the angular momentum cross product $f(i,j)P^iP^j$, where $i+j>3$; $i,j>1$; and $f(i,j)$ is a distortion constant. In this approach, *each* term operates on *all* $|m,K\rangle$ states.[48] However, our attempts to use distortion terms based on such angular momentum cross products never produced fits close to experimental error, and hence we chose to use the distortion terms discussed above.

Since it was not possible to determine V_3 from the data at hand, fits were performed over a range of V_3's. Examination of the sum $\lambda_x^2 + \lambda_z^2$ for a variety of V_3 values showed that the sum increased monotonically with the barrier height, and reached a value of unity near $V_3 = 25.0\ \text{cm}^{-1}$. Hence 25.0 cm^{-1} is taken as an approximate upper limit to V_3. It should be noted that with the current data set, correlations between various parameters only allow us to place limits of $0.0\ \text{cm}^{-1} \leqslant V_3 \leqslant 25\ \text{cm}^{-1}$. However, when $\lambda_x^2 + \lambda_z^2$ was constrained to unity, the standard deviation of the fit was severalfold worse but V_3 was not significantly correlated with other parameters and was determined to be $\sim 10.5\ \text{cm}^{-1}$. Also, the fitted changes in A and Δ_K relative to the $m = 0$ state are significantly lower for $V_3 = 10.5\ \text{cm}^{-1}$ than $V_3 = 0.0\ \text{cm}^{-1}$. Hence we feel $V_3 = 10.5 \pm 5.0\ \text{cm}^{-1}$ is a good estimate of the barrier height. In Tables III and IV fitted parameters for both water tunneling states are reported with V_3 fixed at 10.5 and 0.0 cm^{-1} for comparison.

The nearly constant value of 113 MHz ($\pm$ 3 MHz) between the lower and higher frequency tunneling state transitions along with an approximate 3:1 intensity ratio for lower relative to higher frequency transitions allows the construction of an energy level diagram including the effect of water tunneling. The 3:1 intensity ratio is indicative of an ortho:para partition of the spin states of the water protons. Because the splitting is constant in all of the five pairs of transitions observed, all transitions must be crossing a water tunneling splitting which is *not* a strong function of m or K. Also, because the intensity ratio always favors the lower frequency transitions, we conclude that these transitions are associated with the ortho water spin state. As is discussed in more detail below, the observed selection rules are "top to bottom" and "bottom to top." That is, the lower frequency transitions originate from the upper water tunneling state

TABLE II. Measured *b*–dipole (FIR) transition frequencies (MHz) for the ortho and para water tunneling states of H_3N–HOH.

	K'	K''	m	Ortho measured	o–c[a]	Para measured	o–c[a]
$P(9)$	−1	0	0	531 565.6	1.3		
$P(8)$	−1	0	0	544 107.0	−0.6	544 218.4	−2.0
$P(6)$	−1	0	0	569 103.0	−2.0	569 219.2	−0.2
$P(5)$	−1	0	0	581 555.3	−2.2	581 672.9	0.4
$P(4)$	−1	0	0	593 977.6	−0.7	594 093.9	0.2
$P(3)$	−1	0	0	606 366.3	−0.1	606 484.0	2.0
$P(2)$	−1	0	0	618 720.5	−0.5	618 837.0	0.1
$Q(1)$	1	0	0	643 360.5	1.0	643 474.3	−1.2
$Q(2)$	1	0	0	643 426.7	1.3	643 542.7	1.3
$Q(3)$	1	0	0	643 525.4	1.1	643 641.4	1.2
$Q(4)$	1	0	0	643 657.2	1.1	643 772.6	0.7
$Q(5)$	1	0	0	643 820.7	0.0	643 936.5	0.1
$Q(6)$	1	0	0	644 018.5	0.4	644 134.0	0.3
$Q(7)$	1	0	0	644 248.9	0.5	644 361.4	−2.4
$Q(8)$	1	0	0	644 512.7	1.3	644 627.1	0.6
$Q(9)$	1	0	0	644 807.8	0.8	644 921.9	0.1
$Q(10)$	1	0	0	645 135.2	−0.1	645 249.4	−0.2
$Q(11)$	1	0	0	645 496.3	0.2	645 609.4	−0.4
$Q(12)$	1	0	0	645 888.5	−0.8	646 001.6	−0.7
$Q(13)$	1	0	0	646 314.7	−0.2	646 426.4	−0.5
$Q(14)$	1	0	0	646 772.5	−0.3		
$Q(15)$	1	0	0	647 262.1	−0.6		
$Q(16)$	1	0	0	647 783.6	−1.1		
$Q(17)$	1	0	0	648 336.9	−1.7		
$Q(18)$	1	0	0	648 923.5	−0.6		
$Q(19)$	1	0	0	649 540.8	−0.5		
$Q(20)$	1	0	0	650 189.9	−0.1		
$Q(21)$	1	0	0	650 870.2	0.3		
$Q(22)$	1	0	0	651 582.0	1.0		
$Q(23)$	1	0	0	652 324.1	1.1		
$R(0)$	−1	0	0	655 577.6	1.7	655 692.5	0.8
$R(1)$	−1	0	0	667 790.2	1.8	667 904.2	0.3
$R(2)$	−1	0	0	679 964.6	1.3	680 080.0	1.7
$R(3)$	−1	0	0	692 097.4	−2.2	692 212.8	−1.3
$R(4)$	−1	0	0	704 196.3	−0.3	704 310.3	0.0
$R(5)$	−1	0	0	716 252.1	−1.3	716 364.7	−1.4
$R(6)$	−1	0	0	728 267.2	−1.7	728 377.8	−2.6
$R(7)$	−1	0	0	740 241.9	−0.6	740 353.1	0.5
$R(9)$	−1	0	0	764 059.7	0.0	764 165.1	−1.0
$R(10)$	−1	0	0	775 901.2	−0.3	776 005.3	−0.4
$R(11)$	−1	0	0	787 699.3	1.6	787 802.1	2.8
$P(8)$	0	1	1	534 884.7	2.6	534 995.0	0.2
$P(7)$	0	1	1	547 085.9	1.4	547 196.8	−0.7
$P(5)$	0	1	1	571 512.1	0.7	571 623.5	−1.2
$P(4)$	0	1	1	583 737.9	−1.2	583 851.1	−1.5
$P(3)$	0	1	1	595 977.0	−0.8	596 090.8	−0.5
$P(2)$	0	1	1	608 227.2	−0.8	608 341.1	−0.4
$P(1)$	0	1	1	620 488.8	−1.0	620 603.0	−0.3
$Q(1)$	0	1	1	632 772.2	−0.9	632 885.7	−0.8
$Q(2)$	0	1	1	632 792.5	−0.8	632 906.2	−0.4
$Q(3)$	0	1	1	632 822.2	−0.3	632 935.2	−0.4
$Q(4)$	0	1	1	632 859.1	−0.1	632 973.0	0.8
$Q(5)$	0	1	1	632 901.8	0.0	633 015.0	0.7
$Q(6)$	0	1	1	634 947.9	0.1	633 060.7	0.9
$Q(7)$	0	1	1	632 995.0	0.5	633 107.2	1.2
$Q(8)$	0	1	1	633 040.0	1.2	633 149.5	−0.1
$Q(9)$	0	1	1	633 078.0	0.6	633 187.4	0.3
$Q(10)$	0	1	1	633 107.2	0.9	633 215.1	0.3
$Q(11)$	0	1	1	633 122.1	0.6	633 228.6	0.0
$Q(12)$	0	1	1	633 119.1	0.2	633 224.1	−0.1
$Q(13)$	0	1	1	633 093.1	−1.0	633 197.4	−0.1
$Q(14)$	0	1	1			633 144.0	−0.2
$R(1)$	0	1	1	657 337.9	−0.5	657 453.1	1.5
$R(2)$	0	1	1	669 638.4	0.4	669 750.3	−0.6
$R(3)$	0	1	1	681 943.4	0.7	682 055.7	0.5
$R(4)$	0	1	1	694 247.8	−1.9	694 360.9	−0.8
$R(5)$	0	1	1	706 556.4	0.5	706 668.7	1.5
$R(6)$	0	1	1	718 857.3	−0.5	718 967.5	−0.8

TABLE II. (*Continued.*)

	K'	K''	m	Ortho measured	o–c[a]	Para measured	o–c[a]
$R(7)$	0	1	1	731 150.7	−0.6	731 261.6	0.9
$R(8)$	0	1	1	743 433.9	1.5	743 543.3	3.0
$R(9)$	0	1	1	755 696.7	0.8	755 801.0	−1.4
$R(10)$	0	1	1	767 937.9	0.5	768 041.0	−0.8
$R(11)$	0	1	1	780 151.2	−0.5	780 253.0	−0.7
$R(12)$	0	1	1	792 333.8	0.0		
$R(13)$	0	1	1	804 476.1	−2.5		
$P(7)$	2	1	1	567 441.0	−0.4		
$P(6)$	2	1	1	579 613.7	−0.7	579 730.7	−1.5
$P(5)$	2	1	1	591 811.1	0.9	591 928.4	0.3
$P(4)$	2	1	1	604 024.2	−1.6	604 141.6	−2.2
$P(3)$	2	1	1	616 256.7	−1.9		
$Q(2)$	2	1	1	653 073.0	−1.1	653 192.0	0.2
$Q(3)$	2	1	1	653 109.3	0.0	653 226.4	−0.4
$Q(4)$	2	1	1	653 158.7	0.6	653 279.1	3.6
$Q(5)$	2	1	1	653 222.6	0.0	653 340.4	0.7
$Q(6)$	2	1	1	653 305.6	1.0	653 421.6	0.2
$Q(7)$	2	1	1	653 408.0	1.1	653 524.4	1.1
$Q(8)$	2	1	1	653 533.5	1.3	653 649.2	1.0
$Q(9)$	2	1	1	653 685.6	1.5	653 800.2	0.6
$Q(10)$	2	1	1	653 867.9	1.9	653 981.5	0.6
$Q(11)$	2	1	1	654 082.8	1.2	654 196.7	0.9
$Q(12)$	2	1	1	654 335.2	0.3	654 449.3	1.0
$Q(13)$	2	1	1	654 629.1	−0.6	654 742.3	0.0
$Q(14)$	2	1	1	654 967.9	−2.0	655 080.1	−1.3
$Q(15)$	2	1	1	655 355.7	−3.5		
$R(1)$	2	1	1	677 617.2	−2.0	677 735.9	−0.8
$R(2)$	2	1	1	689 923.4	−1.4	690 041.4	−0.7
$R(3)$	2	1	1	702 241.2	−0.4	702 358.2	−0.3
$R(4)$	2	1	1	714 569.4	−1.1	714 687.3	0.3
$R(5)$	2	1	1	726 913.2	0.5	727 026.2	−2.6
$R(6)$	2	1	1	739 271.3	1.1	739 387.4	1.8
$R(8)$	2	1	1	764 040.3	1.3	764 151.6	−1.2
$R(9)$	2	1	1	776 457.0	1.3	776 567.7	−0.6
$R(10)$	2	1	1	788 898.1	0.6	789 008.6	−0.4
$R(11)$	2	1	1	801 369.5	1.8	801 477.5	−0.3
$P(7)$	1	2	2	536 803.6	2.3		
$Q(2)$	1	2	2	621 577.6	−2.4	621 690.1	0.4
$Q(3)$	1	2	2	621 719.0	−1.6	621 830.6	0.1
$Q(4)$	1	2	2	621 906.2	0.2	622 017.8	1.9
$Q(5)$	1	2	2	622 135.1	0.9	622 244.2	0.0
$Q(6)$	1	2	2	622 404.6	1.8	622 512.8	0.1
$Q(7)$	1	2	2	622 710.4	1.3	622 818.2	−0.6
$Q(8)$	1	2	2	623 050.4	0.7	623 159.6	0.4
$Q(9)$	1	2	2	623 420.2	−0.8		
$Q(10)$	1	2	2	623 815.6	−3.4		
$R(3)$	1	2	2	670 836.5	−3.8	670 947.9	−1.8
$R(4)$	1	2	2	683 294.5	−1.0	683 404.3	−0.4
$R(5)$	1	2	2	695 791.3	4.5	695 894.6	−1.0
$R(6)$	1	2	2	708 311.4	0.9	708 419.6	0.9
$Q(4)$	3	2	2	662 127.5	0.6	662 246.6	−0.1
$Q(5)$	3	2	2	662 376.0	0.2	662 494.7	−0.4
$Q(6)$	3	2	2	662 677.6	−0.3	662 796.1	−0.7
$Q(7)$	3	2	2	663 034.3	−1.0	663 152.6	−1.0
$Q(8)$	3	2	2	663 450.3	0.2	663 566.9	−0.8
$Q(9)$	3	2	2	663 923.2	−1.5	664 041.5	−0.2
$Q(10)$	3	2	2	664 461.5	−0.5	664 577.9	−0.3
$Q(11)$	3	2	2	665 065.5	0.8	665 179.7	−0.5
$Q(12)$	3	2	2	665 736.7	0.5	665 850.8	0.1
$Q(13)$	3	2	2	666 480.3	0.9	666 595.7	2.6
$Q(14)$	3	2	2	667 297.8	0.1	667 410.4	−0.1
$Q(15)$	3	2	2	668 194.3	0.0	668 306.1	−0.2
$Q(16)$	3	2	2	669 171.8	−0.5	669 282.7	−0.7
$R(2)$	3	2	2	698 634.1	0.6	698 754.2	0.9
$R(3)$	3	2	2	711 060.7	−0.5	711 181.6	1.2
$R(4)$	3	2	2	723 537.5	0.4	723 655.9	0.3

[a]Calculated for $V_3 = 10.5\ \mathrm{cm}^{-1}$.

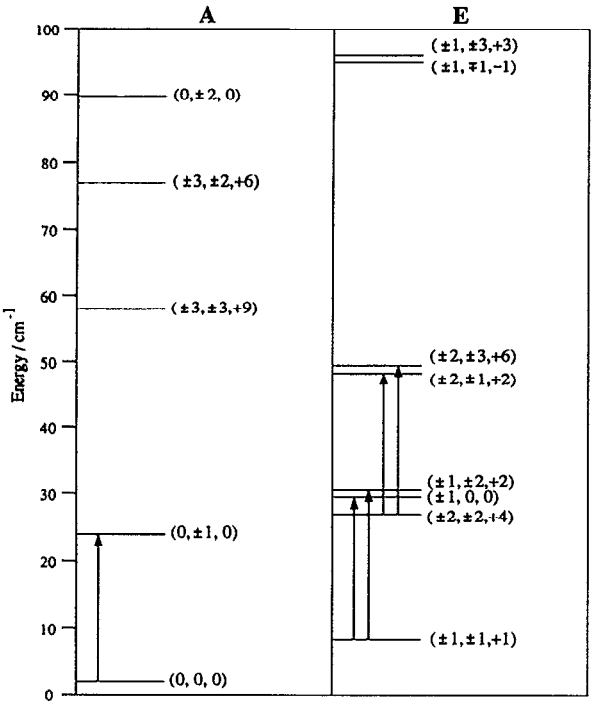

FIG. 5. Energy level diagram for the internal rotor states. Levels are labeled with m, K, and the product mK. Observed transitions are shown with arrows.

and terminate on the lower water tunneling state, while the higher frequency transitions originate from the lower water tunneling state and terminate on the upper water tunneling state. The lower water tunneling state is always spatially symmetric while the upper tunneling state is spatially antisymmetric. Consequently, in order to reproduce both the observed intensity and tunneling splitting data, the pairing of the ortho and water spin functions with the spatial water tunneling functions must be a function of both m and K. Specifically, when $m + K$ is even, the ortho water spin function pairs with a spatially antisymmetric water tunneling function and the para spin function pairs with a spatially symmetric water tunneling function. When $m + K$ is odd, the pairing is reversed. This yields the energy level diagram shown in Fig. 6, which is consistent with the observed spectra.

TABLE III. Fitted spectroscopic constants for the ortho tunneling state of H_3N–HOH.[a] Errors are one standard deviation of the fit.

	$V_3 = 0.0\ cm^{-1}$	$V_3 = 10.5\ cm^{-1}$
A (MHz)	147 709.59(30)	147 608.29(30)
B (MHz)	6 168.864(74)	6 168.860(75)
C (MHz)	6 110.564(49)	6 110.556(49)
Δ_J (kHz)	34.69(15)	34.69(15)
Δ_{JK} (MHz)	1.0243(74)	1.0221(74)
Δ_K (MHz)	70.319(71)	46.215(71)
δ_K (MHz)	− 1.159(24)	− 1.160(24)
H_{JK} (Hz)	− 536.4(96)	− 536.3(96)
H_{KJ} (kHz)	285.3(23)	284.1(23)
λ_x	0.172 70(22)	0.172 89(23)
λ_z	0.981 3315(25)	0.981 9034(25)
$\Delta A_{m=\pm 2}$ (MHz)	653.01(53)	23.08(53)
$\Delta_{K,m=\pm 2}$ (MHz)	97.899(42)	37.341(42)
$\Delta\overline{B}_{\pm 1,\pm 1,+1}$ (MHz)	− 2.089(33)	− 2.084(33)
$\Delta\overline{B}_{\pm 1,0,0}$ (MHz)	− 2.089(33)[b]	− 2.084(33)[b]
$\Delta\overline{B}_{\pm 2,\pm 1,+2}$ (MHz)	6.019(58)	6.009(59)
$\Delta\overline{B}_{\pm 2,\pm 2,+4}$ (MHz)	16.049(94)	16.04(94)
$\Delta\overline{B}_{\pm 2,\pm 3,+6}$ (MHz)	27.67(19)	27.61(20)
$\Delta_{J,\pm 2,\pm 3,+6}$ (kHz)	37.8(17)	37.3(42)

[a] $I_a = 2.7421$ amu Å^2 and $\lambda_y = 0$.
[b] Fixed at the value for $\Delta\overline{B}_{\pm 1,\pm 1,+1}$.

TABLE IV. Fitted spectroscopic constants for the para tunneling state of H_3N–HOH.[a] Errors are one standard deviation of the fit.

	$V_3 = 0.0\ cm^{-1}$	$V_3 = 10.5\ cm^{-1}$
A (MHz)	147 713.78(41)	147 612.51(41)
B (MHz)	6 168.74(10)	6 168.73(10)
C (MHz)	6 110.750(75)	6 110.744(75)
Δ_J (kHz)	34.96(16)	34.95(16)
Δ_{JK} (MHz)	1.070(16)	1.068(11)
Δ_K (MHz)	70.378(64)	46.283(65)
δ_K (MHz)	− 1.288(37)	− 1.289(37)
H_{JK} (Hz)	− 632(37)	− 633(37)
H_{KJ} (kHz)	297.0(29)	295.8(29)
λ_x	0.171 49(31)	0.171 69(31)
λ_z	0.981 3462(35)	0.981 9178(35)
$\Delta A_{m=\pm 2}$ (MHz)	654.25(55)	24.65(55)
$\Delta_{K,m=2}$ (MHz)	98.019(45)	37.490(45)
$\Delta\overline{B}_{+1,+1,+1}$ (MHz)	− 2.123(34)	− 2.118(34)
$\Delta\overline{B}_{\pm 1,0,0}$ (MHz)	− 2.123(34)[b]	− 2.118(34)[b]
$\Delta\overline{B}_{\pm 2,\pm 1,+2}$ (MHz)	5.985(62)	5.974(62)
$\Delta\overline{B}_{\pm 2,\pm 2,+4}$ (MHz)	16.46(12)	16.45(12)
$\Delta\overline{B}_{\pm 2,\pm 3,+6}$ (MHz)	28.64(24)	28.57(24)
$\Delta_{J,\pm 2,\pm 3,+6}$ (kHz)	38.26(22)	38.24(22)

[a] $I_a = 2.7421$ amu Å^2 and $\lambda_y = 0$.
[b] Fixed at the value for $\Delta\overline{B}_{\pm 1,\pm 1,+1}$.

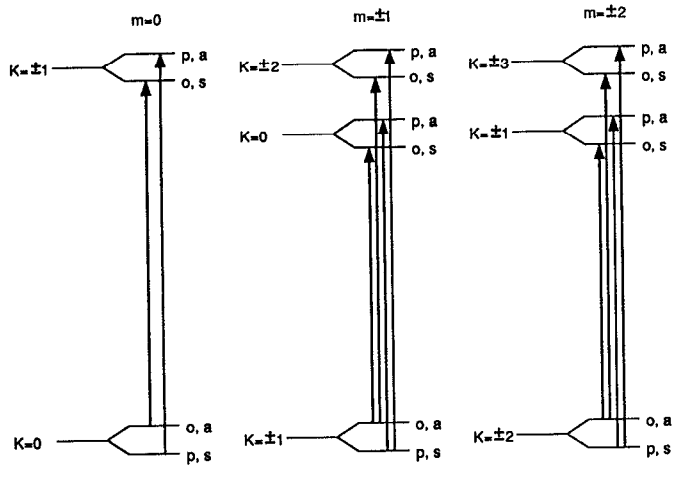

FIG. 6. Energy level diagram for the observed bands showing both the internal rotor and water tunneling states. The ortho and para water proton spin states are indicated by o or p. The symmetry of the water tunneling spatial wave function is given by s or a for symmetric or antisymmetric. Note that the pairing of o/p with s/a is a function of both m and K.

TABLE V. Measured effective dipole moments (Ref. 31) and fitted *a*– and *b*–dipoles.

Transition $(J,M_J \rightarrow J',M'_J)$	μ^a_{eff} (D)	This work	Ref. 31
	H_3N–HOH		
1,0→1,1	2.9788(5)		
2,1→2,2	2.9850(4)	$\mu_a = 2.9763(11)$	$\mu_a = 2.9766(8)$
1,0→0,0	2.9768(3)	$\mu_\perp = 1.18(13)$	$\mu_\perp = 0.52(5)$
2,0→1,1	2.9814(6)		
	D_3N–DOD		
1,0→1,1	3.0149(10)	$\mu_a = 2.9928$	$\mu_a = 2.9928(24)$
1,0→0,0	3.0011(15)	$\mu_\perp = 2.52$	$\mu_\perp = 1.21(8)$

[a] All measured Stark effect data is from Ref. 31.

IV. DIPOLE MOMENTS

HD obtained electric dipole moments for a number of *a*–dipole transitions. The effective dipole moments obtained by them are presented in Table V. The small variations in the effective moments are due to the contribution from the perpendicular dipole. HD used the following approximate equations[31,49] to fit the effective dipole moments:

$$\mu^2_{\text{eff}}(1,0\rightarrow 1,1) = \mu_a^2 + \frac{2}{3}\frac{B+C}{\Delta E}\mu_\perp^2,$$
$$\mu^2_{\text{eff}}(2,1\rightarrow 2,2) = \mu_a^2 + 2\frac{B+C}{\Delta E}\mu_\perp^2, \qquad (11)$$
$$\mu^2_{\text{eff}}(1,0\rightarrow 0,0) = \mu_a^2 + \frac{1}{4}\frac{B+C}{\Delta E}\mu_\perp^2,$$
$$\mu^2_{\text{eff}}(2,0\rightarrow 1,1) = \mu_a^2 + \frac{24}{31}\frac{B+C}{\Delta E}\mu_\perp^2,$$

where $\mu_\perp = \mu_b$ for a C_S structure and ΔE is the separation of the $K=0$ and $K=1$ states. HD used an A value of 153 GHz determined from their structure fits for ΔE. However, the nearly free internal rotation of the ammonia significantly changes the separation of the $K=0$ and $K=1$ levels even when $m=0$. This can be seen from Eq. (4) which shows the contribution to the effective rotational constants due to internal rotation. In H_3N–HOH, the NH_3 C_{3v} axis projects predominately on the a axis of the frame and I_{top} is similar in magnitude to I_α. This results in a large A' and the $m=0$, $K=0$–1 transitions are seen at 643.4 GHz rather than ~150 GHz as would be expected from the structural A value. It should be noted that in their paper on H_3N–H_2S,[34] Herbine *et al.* recognize that the $K=0$ and 1 states in both H_3N–HSH and H_3N–HOH are probably split by more than the structural A value. In fact, a reasonable estimate of the effective A-rotational constant of H_3N–HOH based on a free rotor model is given in this paper. However, since no information was available on the barrier to internal rotation, Herbine *et al.* used the structural A value for ΔE in both H_3N–HSH and H_3N–HOH.

We have refit the H_3N–HOH and D_3N–DOD dipole moment data of Herbine and Dyke using our measured $K=0$–1 separation for H_3N–HOH and a calculated value of 332 GHz for D_3N–DOD. The results of these calculations are reproduced in Table V. For comparison, we have reported the same quantities from the previous work of HD. The *b*–dipole moment obtained using the greater $K=0$–1 spacing is approximately a factor of 2 larger than the value reported by HD. However, there still remains a large discrepancy between the *b*–dipole moments determined for D_3N–DOD and H_3N–HOH. This is most likely due to *b*–dipole connections between states other than $m=0$, $K=1$ and $m=0$, $K=0$. Since $I_\alpha(ND_3) \sim 2I_\alpha(NH_3)$, the density of internal rotor states will be greater for D_3N–DOD. Also, the vibrational levels are lower lying for D_3N–DOD and Eqs. (11) are probably better approximations for H_3N–HOH than for D_3N–DOD. Currently, Stark field plates have been installed about the planar nozzle, and a direct measurement of the *b*–dipole moment will be pursued.

V. STRUCTURAL ANALYSIS

The coordinate system and notation used to describe the complex are shown in Fig. 1 and are the same as were used by HD. The distance between the monomers is specified by $R(N\cdots O)$ and the Euler angles, ϕ, θ, χ for each monomer. The angles are subscripted O or N to denote H_2O or NH_3. Since only five of the six angles are independent, ϕ_O was fixed at zero. As noted earlier by HD, the inertia tensor is invariant to rotation of the ammonia top about its symmetry axis, so no information about the average ammonia conformation is available from the rotational constants, and thus χ_N was also set to zero. This leaves five structural parameters to be determined: $R(N\cdots O)$, θ_N, ϕ_N, θ_O, and χ_O.

The structure published by HD was determined from measured $(B+C)/2$ rotational constants for three isotopomers and the nitrogen quadrupole coupling constant of H_3N–HOH. Since there were only four independent pieces of data, and since the $(B+C)$ values do not depend strongly on ϕ_N, HD set $\phi_N = 0$. The angle between the ammonia symmetry axis and the a axis of the complex, θ_N, was held fixed at 23.1°. The value of θ_N was determined from the nitrogen quadrupole coupling constant of the dimer by the usual method of projecting the free monomer value onto the a axis of the complex. HD then fit $R(N\cdots O)$, θ_O, and χ_O to the three available $(B+C)/2$ values to yield $R(N\cdots O) = 2.983$ Å, $\theta_O = 56°$, and $\chi_O \sim 0°$. This yields a structure with C_S symmetry and a nearly linear hydrogen bond ($\angle$N–O–H = 5°).

Intuition would lead to the prediction of C_S symmetry for the dimer structure. This is borne out in *ab initio* calculations[33] and in the fact that $\lambda_x^2 + \lambda_z^2 \sim 1$. For a C_S structure, only $R(N\cdots O)$, θ_N, and θ_O need to be determined. Our data allows the determination of all three rotational constants for the single isotopomer, H_3N–HOH. In principle, all three structural parameters are obtainable from the rotational constants of H_3N–HOH alone. However, the main contribution to $(B–C)$ is due to the out-of-plane protons on the ammonia and $(B–C)$ is only weakly dependent on θ_N or θ_O. Hence we must fix one of the two angles at a value determined by other data or use data from other isotopomers. Since we have determined λ_z from the internal rotor analysis, we have an independent measure of the average projec-

TABLE VI. Fitted structural parameters for H_3N–HOH and comparison with *ab initio* values.[a]

	(a) $\theta_N = 11.1°$		(b) $\theta_N = 23.1°$	
	θ_O(deg)	R(N···O)(Å)	θ_O(deg)	R(N···O)(Å)
1	−62.9	2.972	−49.2	2.989
2	63.2	2.972	49.8	2.989
3	$\theta_N = 9.5°$	$\theta_O = 59.2°$		R(N···O) = 2.942 Å

[a]Structures (1) and (2) were fit with STRFTQ, consistent with the rotational constants in this work. Residuals of the fits were ~0.03 amu Å^2. Structure (3) values are from *ab initio* equilibrium calculations of Ref. 33.

tion of the ammonia symmetry axis onto the a axis. One method of approximating θ_N is from the measured value of λ_z

$$\lambda_z \simeq \langle \cos\theta_N \rangle \simeq \cos\langle \theta_N \rangle, \tag{12}$$

where the average is taken over the complete vibrational wave function. Using Eq. (12), we obtain $\theta_N^{\lambda_z} = 11°$. This differs significantly from the 23.1° value obtained by simple projection of the free monomer's quadrupole coupling constant onto the dimer a axis (θ_N^{eQq}) and merits some discussion.

The nitrogen quadrupole coupling constant is a measure of $\langle \cos^2\gamma_N \rangle$, while λ_z is a measure of $\langle \cos\gamma_N \rangle$, where γ is the angle between the C_{3v} axis of NH_3 and the a axis of the complex. For a one-dimensional harmonic oscillator in θ with wave functions of the form

$$\Psi = \left(\frac{\alpha}{\pi}\right)^{1/4} e^{-[\alpha(\theta-\theta_{eq})^2]/2}, \tag{13}$$

vibrational averaging yields

$$\langle \cos\theta \rangle \approx \cos\theta_{eq} \cdot e^{-1/4\alpha}, \tag{14}$$

$$\langle \cos^2\theta \rangle \approx \cos^2\theta_{eq} \cdot e^{-1/\alpha} + \tfrac{1}{2}(1 - e^{-1/\alpha}), \tag{15}$$

where it has been assumed that the wave functions are localized enough to allow replacement of $\pm\pi$ in the integration limits with $\pm\infty$. From Eqs. (14) and (15) it can be seen that $\langle \cos\theta \rangle$ lies closer to the value of $\cos\theta_{eq}$ than does $[\langle \cos^2\theta \rangle]^{1/2}$ because of the difference in the exponential factors, $e^{-1/4\alpha}$ vs $e^{-1/2\alpha}$. Hence even for a one-dimensional harmonic oscillator, there is a difference between $\cos^{-1}[\langle \cos \rangle]$ and $\cos^{-1}[\langle \cos^2 \rangle]^{1/2}$.

If the ammonia projection on the a axis were a one-dimensional problem (i.e., $\gamma_N = \theta_N$), Eqs. (14) and (15) would allow an estimation of both $[\theta_N]_{eq}$ and α from the values of $\langle \cos\gamma_N \rangle$ and $\langle \cos^2\gamma_N \rangle$ determined from λ_z and the nitrogen quadrupole coupling constant. However, the angle γ_N is a function of both θ_N and ϕ_N. For H_3N–HOH, the in-plane and out-of-plane NH_3 bending modes are calculated by *ab initio* methods[33] to differ by only 19%. Therefore, the root-mean-square displacement from equilibrium of the ammonia symmetry axis will be similar in both the θ_N and ϕ_N coordinates. Inclusion of out-of-plane vibrational averaging will magnify the difference between and $\cos^{-1}[\langle \cos\gamma_N \rangle]$ and $\cos^{-1}[\langle \cos\gamma_N^2 \rangle]^{1/2}$ and make the extraction of θ from the measurement of these quantities ambiguous.

Because of the uncertainty in the value of $\langle \theta_N \rangle$, we chose to examine structures with θ_N fixed at both 11° and 23°. Fits of θ_O and R(N···O) were performed to the $m = 0$ rotational constants obtained in this work. The FORTRAN

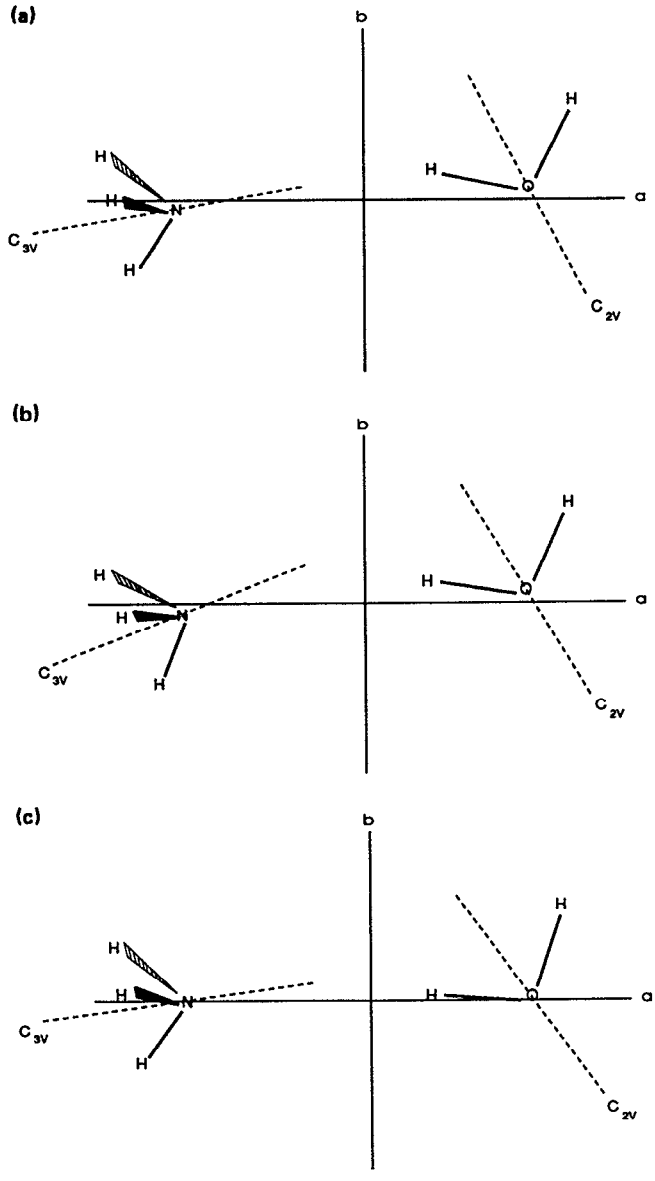

FIG. 7. (a) and (b) are of fitted structures (2a) and (2b) with θ_N held fixed at 11.1° and 23.1°, respectively. Figure (c) is of the *ab initio* equilibrium structure from Ref. 33.

program STRFTQ developed by Schwendeman[50] and later modified by Frank Lovas at NIST, Gaithersburg was used. We made the usual assumption that the structures of the monomers remain unchanged upon complexation. The values of the vibrationally averaged structural constants for water and ammonia were taken from Harmony *et al.*[51] Preliminary surveys of the θ_O parameter space revealed the existence of four structures consistent with the rotational constants for each value of $|\theta_N|$ chosen. Two of these structures had the H_2O protons pointing away from the ammonia and can be discounted by the deuterium substitution measurements of HD. The values of θ_O and $R(N\cdots O)$ for the remaining two structures (1) and (2) are reported in Table VI for (a) $\theta_N = 11°$ and (b) 23°, and also for the *ab initio* calculated equilibrium structure (3).

Of the two remaining fitted structures, (1) and (2), structure (1) points the bonding hydrogen of the water monomer away from the lone pair of the ammonia nitrogen, and conversely, structure (2) aligns them. Calculations on a one-dimensional water tunneling potential (discussed below), indicate the vibrationally averaged in-plane water angle lies within a few degrees of the equilibrium value. Hence we prefer structure (2) since it is similar to the structure obtained by *ab initio* calculations and since it has a more linear hydrogen bond. Structure (2a), with $\theta_N = 11°$ and (2b) with $\theta_N = 23°$ are shown along with the *ab initio* structure (3) in Fig. 7. Comparison of (2a) and (2b) shows very similar values for $R(N\cdots O)$ but significantly different values for θ_O, with (2b) being more linearly hydrogen bonded than (2a). The *ab initio* structure has a θ_N similar to (2a) and θ_O between those of (2a) and (2b); $R(N\cdots O)$ is 0.03 Å less than the experimental value.

The average structure from this work (2a) has an NOH angle of ~13°. If we assume that the change in water HOH angle upon complexation is + 3° as calculated by Latajka *et al.*, we can reduce the average NOH angle to 10°. This compares to an *ab initio* equilibrium value of 4.8°. Evidence for a similarly bent hydrogen bond was also obtained for OC–HOH.[18,23] For OC–HOH, a simple one-dimensional potential was used to model water tunneling splittings,[23] dipole moments and water hyperfine constants in the unsubstituted and deuterated species.[18] From this analysis, a hydrogen bond bent by ~10° at *equilibrium* was suggested. Based on the present data, we suggest a similarly bent hydrogen bond in H_3N–HOH. However, to confirm this suggestion more information on both the in- and out-of-plane bending modes is needed to allow complete vibrational averaging calculations to be performed.

VI. WATER TUNNELING MOTION

The water tunneling splitting of 113 MHz is a measure of the the barrier to H_2O proton exchange. The top-to-bottom, bottom-to-top selection rules for this motion demonstrate that the tunneling motion is in the *a–b* plane of the dimer and give rise to transitions separated by twice the energy level splitting. Consequently, the tunneling energy level splitting should be roughly half of the observed splitting or 56.5 MHz. If we assume the equilibrium position of the water and ammonia monomers are close to their vibrationally averaged positions, then a simple one-dimensional model may be used to *estimate* the barrier to water tunneling. We write the potential as a two term Fourier expansion in the water angle θ_O

$$V(\theta) = (V_1/2)(1 - \cos\theta) + (V_2/2)(1 - \cos 2\theta) \tag{16}$$

and

$$-(V_1/4V_2) = \cos\theta_{eq}, \tag{17}$$

where θ_{eq} is the equilibrium angle which we estimate at 63° from the STRFTQ results. The energy is calculated using the following internal rotor Hamiltonian:

$$\hat{H} = -(h^2/8\pi^2 I_{tunnel})\left(\frac{d^2}{d\theta^2}\right) + V(\theta). \tag{18}$$

If the equilibrium structure is such that the C_{3v} axis of ammonia is at an angle to the *a* axis of the complex, both NH_3 and H_2O must move during water tunneling. We can use a "gear ratio" to reduce the motion to one dimension by writing I_{tunnel}, the moment of inertia for the tunneling motion, as

$$I_{tunnel} = I_c(H_2O) + \alpha I_b(NH_3), \tag{19}$$

where α = (angular displacement of ammonia/angular displacement of water) ~ (11.10°/63.22°) = 0.1756. From this treatment, our estimated barrier height is 704 cm^{-1} and the fitted V_1 and V_2 are 4345 and −2411 cm^{-1}. The effective angles determined from $\langle\cos\theta\rangle$ and $\langle\cos^2\theta\rangle$ averaged over the one-dimensional wave functions are 62.2° and 60.5°. If we assume only water is moving in the tunneling process ($\alpha = 0$), the barrier height is estimated at 840 cm^{-1}.

VII. DISCUSSION AND CONCLUSION

The present work provides direct information on two of the six intermolecular motions in the *gas phase* ammonia–water dimer. Both nearly free internal rotation of the NH_3 and tunneling of the H_2O are observed. In addition, evidence has been presented for a structure with a nonlinear equilibrium hydrogen bond. The internal rotor analysis of the observed bands allows us to estimate the barrier to NH_3 rotation as $V_3 = 10.5 \pm 5.0$ cm^{-1} while the water tunneling splitting of 113 MHz is a measure of the the barrier to H_2O proton exchange. The top-to-bottom, bottom-to-top selection rules for this motion demonstrate that the tunneling motion is in the *a–b* plane of the dimer. A simple one-dimensional model allows us to estimate the barrier to water proton exchange as ~700 cm^{-1}. This compares to a barrier of ~225 cm^{-1} for OC–HOH dimer, which has a similar orientation of monomers but a much larger tunneling frequency of 16.7 GHz,[18] and N_2–HOH,[19] which has a measured tunneling splitting of 31.4 GHz and a calculated barrier height of ~130 cm^{-1}. As expected, these examples show a correlation between binding strength and water tunneling barrier.

In their matrix isolation studies of ammonia-water dimer in Ne at 5.5 K, Engdahl and Nelander[32(b)] measured a band at 19.5 cm^{-1} which they interpreted as a torsion of a linearly (N···H–O) hydrogen bonded water molecule about the *a* axis of the dimer, with the ammonia monomer remaining stationary with respect to the Ne matrix. Based

on the present FIR data, this band could also be ascribed to the superposition of some or all of the observed rotation–tunneling bands, which fall between 20 and 22 cm^{-1}. Engdahl and Nelander[32(b)] further made tentative assignments of bands corresponding to all six intermolecular modes and fit an approximate intermolecular force field to five of the observed bands. However, the out-of-plane ammonia bend and the hydrogen bond stretching frequency are assigned at roughly twice the predicted *ab initio* values.[33] Also, the observed intensity for the band assigned to H-bond stretching motion by Engdahl and Nelander is nearly identical to the observed intensities of the bands assigned as the in-plane water and out-of-plane ammonia bends. The *ab initio* calculations predict the intensity of the stretch at 11 to 30 times less intense than the bends. A reassignment of the matrix data in which the H-bond stretch was not observed, and the mode which was assigned to the stretch is reassigned instead to an ammonia bend would be more consistent with the *ab initio* calculations. Our current work does not provide direct information on these higher frequency vibrations which lie between 100–700 cm^{-1}, a very difficult region of the spectrum in which to work at both high resolution and sensitivity with presently available techniques. We mention the discrepancies between the *ab initio* calculations and the matrix isolation work to point out that at present, even a good estimate of the intermolecular harmonic force field has not been definitively demonstrated. The loftier goal of a multidimensional intermolecular potential (free of matrix perurbations) will require the gas phase observation of all the intermolecular modes at rotational resolution. The present analysis of the rotation–tunneling manifolds in H_3N–HOH, combined with the matrix isolation work, provides a good starting point for such future studies.

ACKNOWLEDGMENTS

This research was supported by grants from the Beckman Institute of Caltech, the NSF (CHEM-8957228), the Packard Foundation, and the Sloan Foundation. Acknowledgment is also made to the Donors of the Petroleum Research Fund, administered by the American Chemical Society, for partial support of this work. We thank P. G. Green for help in the data acquisition and for frequent discussions during the course of this work, T. R. Dyke and co-workers for sharing Ref. 34 prior to publication, F. Lovas for supplying us with his version of STRFTQ, and G. T. Fraser for helpful discussions. We also gratefully acknowledge the support and services rendered by the Caltech staff. Division of Geological and Planetary Sciences, California Institute of Technology, Contribution No. 5049.

[1] F. J. Lovas, R. D. Suenram, G. T. Fraser, C. W. Gillies, and J. Zozom, J. Chem. Phys. **88**, 722(1988).
[2] D. D. Nelson, Jr., G. T. Fraser, and W. Klemperer, Science **238**, 1670(1987).
[3] S. L. Miller, in *Physics and Chemistry of Ice*, edited by E. Whaley, S. J. Jones, and L. W. Gold (Royal Soc. of Canada, Ottawa, 1973), p. 42.
[4] K. Ellsworth and G. Schubert, Icarus **54**, 490(1983).
[5] J. I. Lunine and D. J. Stevenson, Appl. J. Suppl. **58**, 493(1985).
[6] U. C. Singh, P. K. Wiener, J. W. Caldwell, and P. A. Caldwell, AMBER (University of California, San Francisco, 1986).
[7] Biodesign Inc., Pasadena, Ca. 91101. Biograf makes use of the AMBER parameterization of nonbonded and hydrogen bonded interactions.
[8] B. R. Brooks, R. E. Bruccoleri, B. D. Olafson, D. J. States, S. Swaminathan, and M. Karplus, J. Comput. Chem. **4**, 187(1983).
[9] N. L. Allinger, Quantum Chemistry Program Exchange, Dept. of Chemistry, University of Indiana, Bloomington, IN, 1985.
[10] T. R. Dyke, B. J. Howard, and W. Klemperer, J. Chem. Phys. **56**, 2442(1972).
[11] (a) T. J. Balle, Ph. D. thesis, University of Illinois, Urbana-Champaign, Illinois, 1980; (b) T. J. Balle, and W. H. Flygare, Rev. Sci. Instrum. **52**, 33(1981).
[12] An extremely large number of appropriate references exist and the following are only a representative sample. (a) N. Ohashi and A. S. Pine, J. Chem. Phys. **81**, 73(1984); (b) R. E. Miller, Science **240**, 447(1988); (c) A. R. W. Mc Kellar, J. Chem. Phys. **92**, 3261(1990); (d) D. J. Nesbitt, Chem. Rev. **88**, 843(1988); (e) see also *Structures and Dynamics of Weakly Bound Molecular Complexes*, edited by A. Weber (Reidel, Dordrect, 1987), and references therein.
[13] An extremely large number of appropriate references exist and the following are only a representative sample. (a) D. H. Levy, Adv. Chem. Phys. **47**, pt. 1, 323(1981); (b) A. W. Castelman, Jr., and R. G. Keesee, Ann. Rev. Phys. Chem. **37**, 525(1986); (c) A. Amirav, U. Even, and J. Jortner, Chem. Phys. Lett. **67**, 9(1979); J. Chem. Phys. **75**, 2489(1981); (d) E. R. Bernstein, K. Law, and M. Schauer, *ibid.* **80**, 634(1984); (e) K. Godzik, T. R. Hays, W. E. Henke, H. L. Selzle, and E. W. Schlag, Laser Chem. **1**, 59(1982).
[14] (a) J. M. Hutson, J. Chem. Phys. **89**, 4550(1988); (b) R. L. Robinson, D.-H. Gwo, and R. J. Saykally, Mol. Phys. **63**, 1021(1988).
[15] R. C. Cohen and R. J. Saykally, J. Phys. Chem. **94**, 7991(1990), and references therein.
[16] P. R. Bunker, V. C. Epa, P. Jensen, and A. Karpfen, J. Mol. Spectrosc. **146**, 200(1991).
[17] S. Suzuki, R. E. Bumgarner, P. A. Stockman, P. G. Green, and G. A. Blake, J. Chem. Phys. **94**, 824(1991).
[18] R. E. Bumgarner, S. Suzuki, P. A. Stockman, P. G. Green, and G. A. Blake, Chem. Phys. Lett. **176**, 123(1991).
[19] R. E. Bumgarner, J. Bowen, and G. A. Blake, at the Forty-fifth Symposium on Molecular Spectroscopy, Columbus, OH, June 16–20, 1990; J. Chem. Phys. (in preparation)
[20] S. Suzuki, P. G. Green, R. E. Bumgarner, and G. A. Blake (to be published).
[21] (a) L. H. Coudert and J. T. Hougen, J. Mol. Spectrosc. **139**, 259(1990). An analysis of the large body of previous microwave and FIR data with reference to IR experiments as well; (b) E. Zwart, J. J. Ter Meulen, and W. Leo Meerts, Chem. Phys. Lett. **166**, 500(1990); (c) **173**, 115(1990).
[22] E. Zwart, Ph.D. thesis, University of Nijmegen, the Netherlands, 1990.
[23] D. J. Yaron, K. I. Peterson, D. Zolandz, W. Klemperer, F. J. Lovas, and R. D. Suenram, J. Chem. Phys. **92**, 7095(1990).
[24] H. O. Leung, M. D. Marshall, R. D. Suenram, and F. J. Lovas, J. Chem. Phys. **90**, 700(1989).
[25] R. C. Cohen, C. A. Schmuttenmaer, K. L. Busarow, and R. J. Saykally (to be published).
[26] S. E. Novick, K. R. Leopold, and W. Klemperer, in *Atomic and Molecular Clusters*, edited by E. R. Bernstein (Elsevier, New York, 1989).
[27] G. T. Fraser, K. R. Leopold, and W. Klemperer, J. Chem. Phys. **81**, 2577(1984).
[28] G. T. Fraser, D. D. Nelson, Jr., G. J. Gerfen, and W. Klemperer, J. Chem. Phys. **83**, 5442(1985).
[29] G. T. Fraser, F. J. Lovas, R. D. Suenram, D. D. Nelson, Jr., and W. Klemperer, J. Chem. Phys. **84**, 5983(1988).
[30] G. T. Fraser, R. D. Suenram, F. J. Lovas, and W. J. Stevens, Chem. Phys. **125**, 31(1988).
[31] P. Herbine and T. R. Dyke, J. Chem. Phys. **83**, 3768(1980).
[32] (a) B. Nelander and L. Nord, J. Phys. Chem. **86**, 4375(1982); (b) A. Engdahl and B. Nelander, J. Chem. Phys. **91**, 6604(1989).
[33] Z. Latajka and S. Scheiner, J. Phys. Chem. **94**, 217(1990), and references therein.
[34] P. Herbine, T. A. Hu, G. Johnson, and T. R. Dyke, J. Chem. Phys. **93**, 5485(1990).
[35] K. L. Busarow, G. A. Blake, K. B. Laughlin, R. C. Cohen, Y. T. Lee, and

R. J. Saykally, J. Chem. Phys. **89**, 1268(1988).
[36] J. Farhoomand, G. A. Blake, M. A. Ferking, and H. M. Pickett, J. Appl. Phys. **57**, 1763(1985).
[37] G. A. Blake, K. B. Laughlin, R. C. Cohen, K. L. Busarow, D.-H. Gwo, C. A. Schmuttenmaer, D. W. Steyert, and R. J. Saykally, Rev. Sci. Instrum. **62**, 1693(1991).
[38] G. A. Blake, K. B. Laughlin, R. C. Cohen, K. L. Busarow, D.-H. Gwo, C. A. Schmuttenmaer, D. W. Steyert, and R. J. Saykally, Rev. Sci. Instrum. **62**, 1701(1991).
[39] R. E. Bumgarner and G. A. Blake, Chem. Phys. Lett. **161**, 308(1989).
[40] D. H. Martin and E. Puplett, Infrared Phys. **10**, 105(1970).
[41] P. R. Bunker, *Molecular Symmetry and Spectroscopy* (Academic, San Diego, 1979).
[42] N. Ohashi and J. T. Hougen, J. Mol. Spectrosc. **121**, 474(1987).
[43] J. T. Hougen, J. Mol. Spectrosc. **114**, 395(1985).
[44] L. H. Coudert and J. T. Hougen, J. Mol. Spectrosc. **130**, 86(1988).
[45] B. L. Crawford, J. Chem. Phys. **8**, 273(1940).
[46] P. H. Turner, M. J. Corkill, and A. P. Cox, J. Phys. Chem. **83**, 1473(1979). Note that there is a slight misprint in this paper as the term $+ V_3/2$ is missing in the diagonal matrix element of Eq. (5) of the reference. See Eq. (5) of this paper.
[47] J. K. G. Watson, in *Vibrational Spectra and Structure*, Vol. 6, edited by J. R. Durig (Elsevier Science, New York, 1977), p. 2.
[48] See, for example, the microwave analyses of nitromethane (a) and methanol (b). (a) F. Rohart, J. Mol. Spectrosc. **57**, 301(1975); (b) F. C. DeLucia, E. Herbst, and T. Anderson, *ibid.* **134**, 395(1989).
[49] A. E. Barton, D. J. B. Howlett, and B. J. Howard, Mol. Phys. **41**, 619(1980).
[50] R. H. Schwendeman, in *Critical Evaluation of Chemical and Physical Structural Information*, edited by D. R. Lide, Jr. and M. A. Paul (National Academy of Sciences, Washington, D.C., 1974).
[51] M. D. Harmony, V. W. Laurie, R. L. Kuczkowski, R. H. Schwendeman, D. A. Ramsay, F. J. Lovas, W. J. Lafferty, and A. G. Maki, J. Phys. Chem. Ref. Data **8**, 619(1972).